Optics Letters

Autofocusing optical-resolution photoacoustic endoscopy

KEDI XIONG, SIHUA YANG,* XIAOWAN LI, AND DA XING

MOE Key Laboratory of Laser Life Science and Institute of Laser Life Science, College of Biophotonics, South China Normal University, Guangzhou 510631, China
**Corresponding author: yangsh@scnu.edu.cn*

Received 13 February 2018; revised 5 March 2018; accepted 17 March 2018; posted 19 March 2018 (Doc. ID 323124); published 11 April 2018

Photoacoustic (PA) endoscopy has the potential to diagnose early diseases in the gastrointestinal tract. For the first time, to our knowledge, we developed an autofocusing PA endoscope (AF-PAE) for the usually irregular gastrointestinal tract imaging to solve the deterioration of transverse resolution caused by the defocus scanning of the probe. The 9-mm-diameter AF-PAE probe integrated a 6-mm aspheric lens and 6-mm liquid lens to automatically adjust the optical focal length, and an unfocused ultrasonic transducer with a center frequency of 15 MHz is coaxially set for detecting PA signals. With this probe, the AF-PAE achieved a focus-shifting range from approximately 2 to 10 mm with high transverse resolution and image contrast in a 360° field of view. Phantom experiment and vasculature distribution of a resected rabbit rectum have been performed to demonstrate the imaging ability of the AF-PAE for potential clinical applications in colorectal vessel imaging and subsequent diagnosis.

OCIS codes: (170.0170) Medical optics and biotechnology; (170.5120) Photoacoustic imaging; (170.2150) Endoscopic imaging.

https://doi.org/10.1364/OL.43.001846

Photoacoustic endoscopy (PAE) that embodies PA imaging in a miniaturized probe can provide high-resolution imaging of internal organs with optical absorption contrast based on its strong spectroscopic imaging capability and high penetration [1–3] and enable structural and functional information by visualizing blood vasculature *in vivo* [4]. In recent years, a number of miniaturized PA endoscopic probes have been reported for various applications, such as intravascular [5–10], gastrointestinal tract [11,12], ovarian cancer [13], bladder [14], and urogenital [15] imaging. Several groups developed miniaturized endoscopic probes for vessel imaging without light converging, but the resolution was limited by the center frequency, bandwidth, and acoustic size of the transducer [11,12]. To improve the spatial resolution, others achieved optical resolution by using a combination of a gradient index lens and single-mode optical fiber, replacing a multimode optical fiber and sacrificing imaging depth [16–19]. However, in clinical applications, the irregular shape of the gastrointestinal tract results in the defocus scanning of the probe. Therefore, the transverse resolution and image contrast deteriorate rapidly as the focus moves away from the target, which results in the deficiency of fine structure imaging.

None of the current PA endoscopic imaging probes using external or internal motorized rotators can meet the requirement of high-resolution imaging in the irregular gastrointestinal tract due to their single focal length and the irregularly shaped target. These probes may not be suited for clinical gastrointestinal tract vessel imaging. Mechanical scanning can improve focal length of the system by moving the objective with a motor-driven linear platform or piezoelectric z-focusing device in the depth direction to meet the requirement of depth scanning. But the focus-shifting speed is limited by mechanical inertia of these moving devices. In order to achieve a fast inertia-free scan, the chromatic aberration has been exploited in PA microscopy (PAM). The limitation of the system is that only a few discrete focus depths can be obtained. Moreover, fast focus-shifting methods have been developed for increasing the depth of focus in PAM by using liquid lenses, multiple acousto-optic detectors (AODs), and liquid acoustic lenses [20–23]. However, unlike the goal of these methods used in PAM, PA endoscopes need a fast focus-shifting method to adjust the focus at the irregular target boundary. Moreover, to our knowledge, there are no reports regarding fast focus-shifting methods in PAE to achieve high spatial resolution PA images in a 360° field of view.

In this Letter, seeking to apply PAE for colorectal vessel imaging, we report our implementation of a fully encapsulated PA endoscopic imaging probe with an integrated liquid lens. The probe achieved dynamic adjustment of focal length and focus tracking of the target boundary based on the PA signal feedback, we believe for the first time. Subsequent experiments demonstrated the development of autofocusing PAE (AF-PAE) for irregular gastrointestinal tract vessel imaging with high spatial resolution and image contrast. Compared with the previous single focal length PAE (SFL-PAE), the AF-PAE can solve the problem that the transverse resolution and image contrast deteriorate rapidly due to the defocus scanning of the probe in an irregularly shaped cavity.

Figure 1(a) shows the schematic of the AF-PAE system, comprising a laser source, an amplifier, a graphics processing

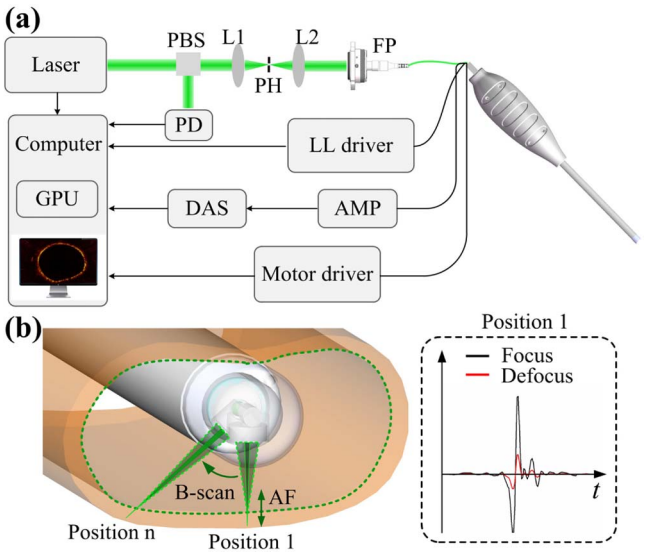

Fig. 1. Schematic of the AF-PAE system. (a) Schematic illustration of the imaging setup. PBS, polarizing beam-splitting prism; PH, pinhole; PD, photodiode; LL driver, liquid lens driver; FP, fiber port; DAS, data acquisition system; AMP, amplifier; GPU, graphics processing unit. (b) Principle of the AF-PAE.

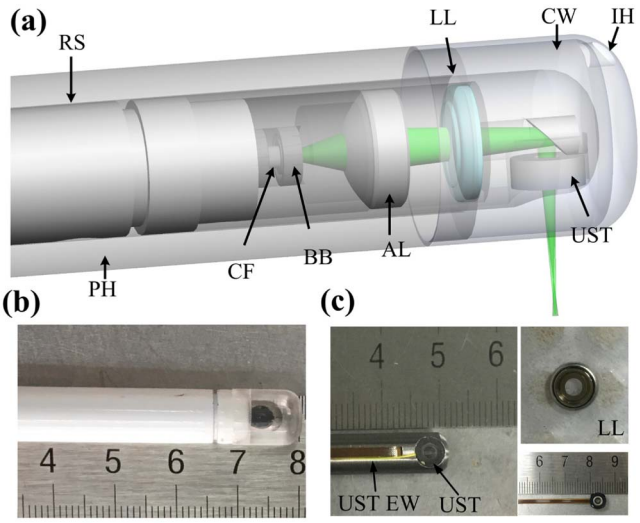

Fig. 2. Structure and components of the imaging probe. (a) Details of the AF-PAE probe. RS, rotating shaft; LL, liquid lens; CW, coupling window; IH, inject hole; PH, plastic housing; BB, ball bearing; CF, ceramic ferrule; AL, aspheric lens; UST, ultrasonic transducer. (b) Photograph of the probe. (c) Photographs of the assembled imaging probe; UST EW, ultrasonic transducer electric wire.

unit (GPU) for image reconstruction, a data acquisition system (DAS), and a computer for displaying images. The laser source with a repetition rate of 10 kHz provides a 527-nm wavelength pulse laser with pulse width of ~7 ns. The transmission pulses are monitored by a photodiode and focused into a 30-μm-diameter pinhole by a convex lens for spatial filtering, collimated by another convex lens, and coupled into the endoscope's single-mode fiber (SMF) via a fiber port (PAF-X-7-A, Thorlabs). A high-speed digitizer (Mi4110, Spectrum, Inc.) at the sampling rate of 100 MS/s is utilized to record PA signals. The recorded PA signals were transfered to the GPU to reconstruct the PA image. The reconstructed images were returned from GPU to the computer for real-time display. Figure 1(b) presents the principle of AF-PAE. There is a great difference in PA signal amplitude excited by the same laser energy between the light converging and light focusing, as PA signal amplitude is proportional to optical density. Therefore, the variation trend of light focusing can be speculated by the signal-to-noise rate (SNR) of the PA signal. Meanwhile, the time-domain distance of the PA signal reflects the focal length. Based on the maximum signal amplitude and the distance between the target surface and the ultrasonic transducer during the focusing process, the AF-PAE can determine the focal length. Considering the imaging in the irregular gastrointestinal tract and the small size of the light spot, 1000 A-lines per B-scan are recorded to obtain a high-quality PA image, which yields an angular step size of 0.36° for the scanning motor.

The details of the imaging probe are illustrated in Fig. 2(a). The 9-mm outer diameter of the probe is made of acrylonitrile butadiene styrene copolymer, a hard plastic material. A transparent dome-shaped distal end was fabricated for light illumination and ultrasound reception. Meanwhile, an injection hole of 1-mm diameter located at the top of the distal end is designed to inject the deionized water or ultrasonic coupling agent into the cavity of the probe and provides acoustic coupling between the imaging window and transducer. Owing to sealed air pressure, the coupling medium will not leak into the tube. The dome-shaped imaging window avoids direct contact of the scanning tip with the target tissue during mechanical scanning. A SMF, the end of which is encapsulated by a customized ceramic ferrule with an outer diameter of 1 mm, is used to deliver light. The ceramic ferrule is held in two multiple ball bearings to provide a free rotation to the probe shell only, separating it from the SMF and over the 1-cm-long tubular section. The laser beam is focused by an aspheric lens (A390-A, Thorlabs) and then adjusted by a liquid lens (Arctic 16F0, Varioptic). A customized 45° mirror at the center of the stainless steel shell is used to reflect the laser beam to the target tissue. All the components are fixed coaxially in a stainless steel shell tube. A customized unfocused ultrasonic transducer with a center frequency of 15 MHz and a bandwidth of 71% is used to detect the PA signals. The transducer's element is a ring with an outer diameter of 5 mm and an inner diameter of 2.5 mm. An optical column with an outer diameter of 2.5 mm is coaxially fixed in the hole of the transducer to prevent the coupling medium from leaking into the tube. To get a three-dimensional PA image, the entire probe was mounted on a one-dimensional linear stage and pulled back with a step of 30 μm. The PA signals were amplified (LNA-650 amplifier, RF Bay, Inc.) at 50 dB. Figures 2(b) and 2(c) show the photographs of the imaging probe and liquid lens. The liquid lens has an aperture size of 1.6 mm and provided a diopter from −20 to +20 as the direct voltage (DC) is driven from 0 to 51 V. We conducted the optical simulation using Zemax software, according to the parameter of the aspheric lens and liquid lens. The distance between the aspheric lens and liquid lens is 1.5 mm. The focus locates at about 2 mm from the coupling window as the control voltage is 51 V. The focal length increases as the control voltage reduces. In AF-imaging mode, the direct voltage of liquid lens was driven from 51 to

0 V per A-line, and the focal length is automatically adjusted based on the maximal SNR of the PA signals in the time-domain distance.

Five tungsten wires were placed in agar phantom, then moved away gradually from the center of phantom, to evaluate the spatial resolution of the AF-PAE system in different depths. Figure 3(a) shows the focal length of the AF-PAE versus the DC voltage. The SFL and AF-PAE imaging were then conducted for comparison. As seen in Fig. 3(b), due to the deviation from the optical focus position, the optical converging degrades, deteriorating the lateral resolution. However, clearly, as the tungsten wires moved away from the probe, the AF PA image of tungsten wires did not disperse. Figures 3(c) and 3(d) present the transverse pixel width of the tungsten wires, corresponding to Fig. 3(b). The transverse pixel width was utilized as the transverse line spread functions (LSPs) to evaluate the transverse resolution. Based on the LSPs, the best transverse resolution is 49 μm. In the radial direction, the resolution depends on the bandwidth and center frequency of the ultrasonic transducer. Figure 3(e) shows the Hilbert-transformed signal of a typical PA A-line signal as the radial LSPs of the target located at the focal point. The full width at half-maximum (FWHM) of the radial profile is ~121 μm, which agrees well with the theoretical radial resolution (117 μm) [24]. Practically, the measured transverse resolution was worse than the theoretical resolution stimulated by Zemax. We speculate that the discrepancy was caused by the position deviation between the aspheric lens and liquid lens and the distortion of acoustic waves by the coupling window. Figure 3(f) presents the transverse resolution of SFL and AF imaging versus the radial distance. The transverse resolution of SFL imaging deteriorates to 300 μm. Despite the decline of the numerical aperture, the transverse resolution of AF-imaging mode still reaches 90 μm in several-millimeter depths, a much better resolution than that of SFL. The acquisition times are about 33 s and 33 ms for a B-can and A-line, due to the response time of liquid lens. The output energy is 2 μJ, which yields a surface fluence of ~11 mJ/cm^2, half of the ANSI safety limit (20 mJ/cm^2) [17].

Figure 4(a) shows schematic illustration of the phantom experiment. The imitated leaf veins were bent in an agar phantom in a transverse direction. The center of the leaf veins was close to the transducer, whereas the edge was far away from the transducer. Four hundred B-scans were obtained to recover a volume-rendered PA image with the focal length of 2, 6, and 10 mm, respectively. Figure 4(b) presents three SFL-PAE volume-rendered images of leaf vein phantoms. As the focus moves away from the transducer, the clear area in the PA volume-rendered image transfers from the chief vein to the edge vein. Figure 4(c) presents radial-maximum amplitude projection (RMAP) images of dashed boxes in Fig. 4(b). Obviously, the partial RMAP images at the focal length of 2 mm is much clearer than that of the out-of-focus area. The transverse resolution and image contrast of veins are decreased, and the shape disperses from line to block. Figure 4(d) shows the RMAP image of the volume-rendered image in AF-imaging mode, which has a high transverse resolution both in the chief and the edge veins. Four subimages of dashed boxes are enlarged to clearly show the vein distribution. However, there is still a small region of the edge veins with lower resolution and contrast. The reason for this is that the longitudinal range of the veins reaches about 8 mm. In this case, as the focus

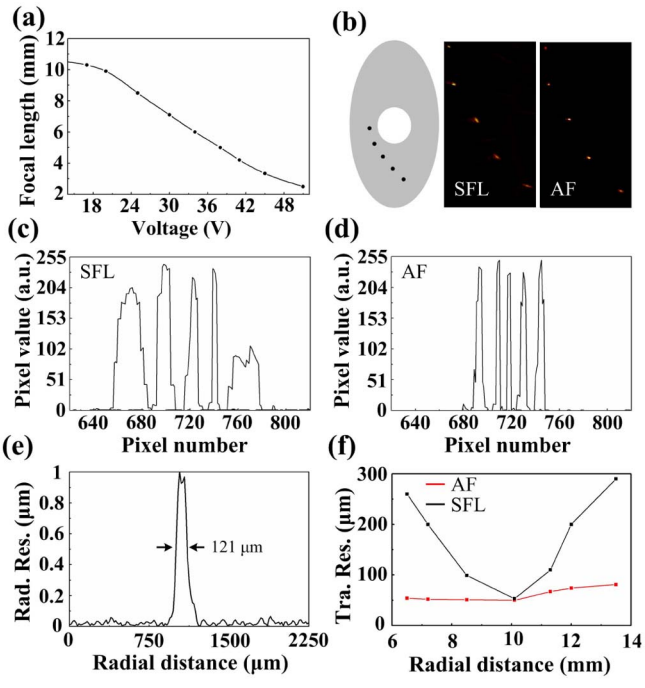

Fig. 3. Resolution evaluation of the AF-PAE performance. (a) The focal length of AF-PAE versus the control voltage. (b) PA images of the 20-μm-thick tungsten wire located at five locations by SFL mode and AF mode. (c), (d) Transverse pixel value of tungsten wires corresponding to (b). (e) FWHM of the radial profile of a typical PA signal. (f) The transverse resolutions of SFL and AF versus the radial distance.

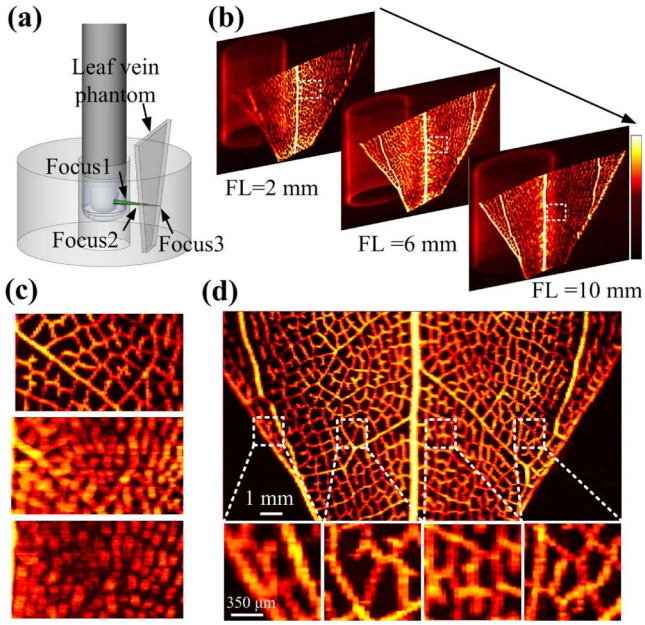

Fig. 4. Phantom imaging results obtained by SFL and AF-imaging mode. (a) Schematic illustration of the experiment. (b) Volume-rendered images of leaf vein at three focal lengths. (c) Representative maximum amplitude projection (MAP) images, corresponding to dashed boxes in (b) with FL = 2, 6, 10 mm, respectively. (d) MAP image of PA volume-rendered image obtained by AF and an enlarged view of the dashed boxes.

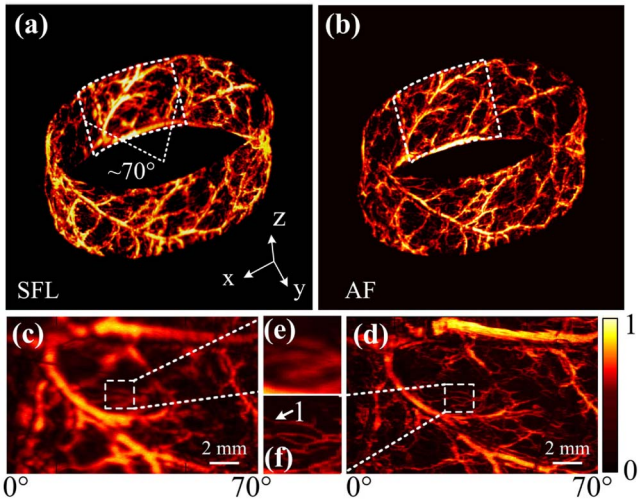

Fig. 5. PA imaging of a rabbit's rectum. (a), (b) Three-dimensional volume-rendered images of SFL and AF. (c), (d) The enlarged-view images of dashed rectangles in (a) and (b). (e), (f) The enlarged-view images of dashed boxes in (c) and (d).

moves away, the numerical aperture of the focused light declines and results in the degradation of transverse resolution and image contrast.

To further demonstrate the feasibility of using the probe on biological tissues, a New Zealand White rabbit was sacrificed and a piece of rectum tissue was dissected. All procedures were approved by the South China Normal University (SCNU). A section of rectum tissue was placed in a hollow elliptical phantom. The radii of the elliptical phantom were about 14.5 and 7 mm in the long axis and short axis direction, respectively. The AF process was conducted per 10 A-lines to reduce the acquisition time, and we consider the distance between the target and transducer varies little in 10 A-lines. Figures 5(a) and 5(b) present volume-rendered images recovered by 400 B-scans with a step size of 30 μm. Figure 5(d) shows the RMAP images of dashed boxes in Fig. 5(b), clearly revealing vasculature distributed in the rectum, whereas the RMAP of vasculature distribution in Fig. 5(c) cannot be distinguished in nearly half of the full field of view in Fig. 5(a). The blood vessel diameter of arrow 1 in Fig. 5(f) was estimated to be about 65 μm, which is comparable to the experimentally quantified spatial resolution value. Meanwhile, the vascular branch in Fig. 5(e) cannot be recognized, as clearly distinguished in the same area in Fig. 5(f). Note that the vasculature distribution appeared to have some discontinuity in both Figs. 5(c) and 5(d); we speculate that the distortions were caused by the blood loss *ex vivo*.

In summary, we developed an AF-PAE that provides a focal dynamic adjustment range from 2 to 10 mm in a 360° field of view. The AF-PAE achieves a relatively high resolution of 49 μm and works well for phantom and *ex vivo* experiments. Unlike conventional PAEs, which work at a single focal length, the AF-PAE has the advantage of autofocusing on the first layer or other layers based on the amplitude variation of the first signal peak or other signal peaks in A-lines, and it can solve the rapid deterioration of transverse resolution as the focus moves away from the target boundary. It should be noted that the transverse resolution still deteriorates as the focal length is increasing. In the future, an optimized combination of lens set and liquid lens may be used to further improve the transverse resolution. Using a quicker fast-response focus-shifting method and multiparameter algorithm (amplitude and frequency) may reduce the time of the AF process and meet the real-time imaging needs. Moreover, *in vivo* early gastrointestinal tumor experiments may be conducted to evaluate the imaging ability in clinical gastrointestinal tract applications. Our first clinical goal is to apply this method for imaging colorectal tumors. As the AF-PAE achieves the method for increasing the transverse resolution over the entire radial imaging range, it would provide more accurate assessments of tumor boundary, growth, and surrounding vascular systems.

Funding. National Natural Science Foundation of China (NSFC) (11774101, 61627827, 81630046, 91539127, 11604105); Science and Technology Planning Project of Guangdong Province, China (2015B020233016); Distinguished Young Teacher Project in Higher Education of Guangdong, China (YQ2015049); Science and Technology Youth Talent for Special Program of Guangdong, China (2015TQ01X882).

REFERENCES

1. V. Ntziachristos, Nat. Methods **7**, 603 (2010).
2. L. V. Wang and S. Hu, Science **335**, 1458 (2012).
3. A. Taruttis and V. Ntziachristos, Nat. Photonics **9**, 219 (2015).
4. J. Yang, C. Favazza, R. Chen, J. Yao, X. Cai, K. Maslov, Q. Zhou, K. Shung, and L. Wang, Nat. Med. **18**, 1297 (2012).
5. X. Bai, X. Gong, W. Hau, R. Lin, J. Zheng, C. Liu, C. Zeng, X. Zou, H. Zheng, and L. Song, PLoS ONE **9**, e92463 (2014).
6. X. Ji, K. Xiong, S. Yang, and D. Xing, Opt. Express **23**, 9130 (2015).
7. J. Zhang, S. Yang, X. Ji, Q. Zhou, and D. Xing, J. Am. Coll. Cardiol. **64**, 385 (2014).
8. M. Wu, G. Springeling, M. Lovrak, F. Mastik, S. Iskander-Rizk, T. Wang, H. van Beusekom, A. van der Steen, and G. V. Soest, Opt. Express **8**, 943 (2017).
9. Z. Piao, T. Ma, J. Li, M. Wiedmann, S. Huang, M. Yu, K. Shung, Q. Zhou, C. Kim, and Z. Chen, Appl. Phys. Lett. **107**, 083701 (2015).
10. J. Hui, Y. C. Cao, Y. Zhang, A. Kole, P. Wang, G. Yu, G. Eakins, M. Sturek, W. Chen, and J. Cheng, Sci. Rep. **7**, 1417 (2017).
11. J. Yang, C. Li, R. Chen, Q. Zhou, K. Shung, and L. Wang, J. Biomed. Opt. **19**, 066001 (2014).
12. J. Yang, R. Chen, C. Favazza, J. Yao, C. Li, Z. Hu, Q. Zhou, K. Shung, and L. Wang, Opt. Express **20**, 23944 (2012).
13. Y. Yang, X. Li, T. Wang, P. Kumavor, A. Aguirre, K. Shung, Q. Zhou, M. Sanders, M. Brewer, and Q. Zhu, Biomed. Opt. Express **2**, 2551 (2011).
14. S. Chen, Z. Xie, T. Ling, L. Guo, X. Wei, and X. Wang, Opt. Lett. **37**, 4263 (2012).
15. C. Li, J. Yang, R. Chen, C. Yeh, L. Zhu, K. Maslov, Q. Zhou, K. Shung, and L. Wang, Opt. Lett. **39**, 1473 (2014).
16. B. Dong, S. Chen, Z. Zhang, C. Sun, and H. Zhang, Opt. Lett. **39**, 4372 (2014).
17. J. Yang, C. Li, R. Chen, B. Rao, J. Yao, C. Yeh, A. Danielli, K. Maslov, Q. Zhou, K. Shung, and L. Wang, Biomed. Opt. Express **6**, 918 (2015).
18. H. Guo, G. Song, H. Xie, and L. Xi, Opt. Lett. **42**, 4615 (2017).
19. N. Liu, S. Yang, and D. Xing, Opt. Lett. **43**, 138 (2018).
20. B. Li, H. Qin, S. Yang, and D. Xing, Opt. Express **22**, 20130 (2014).
21. C. Song, L. Xi, and H. Jiang, Opt. Lett. **38**, 2930 (2013).
22. L. Xi, C. Song, and H. Jiang, Opt. Lett. **39**, 3328 (2014).
23. S. Yang, W. Qin, H. Guo, T. Jin, N. Huang, M. He, and L. Xi, Biomed. Opt. Express **8**, 2756 (2017).
24. S. Mattison, R. Shelton, R. Maxson, and B. Applegate, Biomed. Opt. Express **4**, 1451 (2013).